

Corrugation-dominated mechanical softening of defect-engineered graphene

Wael Joudi^{1,2,*}, Rika Saskia Windisch³, Alberto Trentino^{1,2}, Diana Propst^{1,2}, Jacob Madsen¹, Toma Susi¹, Clemens Mangler¹, Kimmo Mustonen¹, Florian Libisch³ and Jani Kotakoski^{1,*}

¹University of Vienna, Faculty of Physics, Boltzmanngasse 5,
1090 Vienna, Austria

²University of Vienna, Vienna Doctoral School in Physics, Boltzmanngasse 5,
1090 Vienna, Austria

³Institute for Theoretical Physics, Faculty of Physics, Technical University of Vienna,
Wiedner Hauptstrasse 8-10, 1040 Vienna, Austria

*Email: wael.joudi@univie.ac.at, jani.kotakoski@univie.ac.at

(Dated: December 9, 2024)

We measure the two-dimensional elastic modulus E^{2D} of atomically clean defect-engineered graphene with a known defect distribution and density in correlated ultra-high vacuum experiments. The vacancies are introduced via low-energy (< 200 eV) Ar ion irradiation and the atomic structure is obtained via semi-autonomous scanning transmission electron microscopy and image analysis. Based on atomic force microscopy nanoindentation measurements, a decrease of E^{2D} from 286 to 158 N/m is observed when measuring the same graphene membrane before and after an ion irradiation-induced vacancy density of 1.0×10^{13} cm⁻². This decrease is significantly greater than what is predicted by most theoretical studies and in stark contrast to some measurements presented in the literature. With the assistance of atomistic simulations, we show that this softening is mostly due to corrugations caused by local strain at vacancies with two or more missing atoms, while the influence of single vacancies is negligible. We further demonstrate that the opposite effect can be measured when surface contamination is not removed before defect engineering.

Experiments by Lee *et al.* revealed the exceptionally high intrinsic stiffness of monolayer graphene in 2008 [1] based on atomic force microscopy (AFM) nanoindentation. The 2D elastic modulus E^{2D} was reported to be 340 N/m, which corresponds to a Young's modulus of 1 TPa assuming the inter-layer distance of graphite can be used as the thickness of graphene. Several studies [2–18] have also explored the impact of lattice imperfections on the mechanical properties of graphene. However, the results are not fully consistent.

Specifically, vacancy-type defects introduced via low energy Ar ions have been reported to increase E^{2D} up to a maximum of 550 N/m at 0.2% vacancy concentration (after which it decreases again) [13]. In contrast, low irradiation fluence with oxygen plasma was shown to not cause a clear change in E^{2D} , while at higher fluences E^{2D} starts to decrease [12]. Moreover, for boron-doped graphene, an immediate decrease

in E^{2D} was reported after the transition from substitutional defects to vacancies [18]. Similarly, simulations predict different outcomes for defect-engineered graphene. Although most computational studies show a gradual decrease in E^{2D} with increasing vacancy density [2–11], also an increase has been reported at low vacancy densities [15, 19]. However, interestingly, corrugation results in a more drastic decrease of E^{2D} [16, 17, 20, 21].

In this study, we determine the relationship between the exact atomic structure of defect-engineered graphene and its 2D elastic modulus combining scanning transmission electron microscopy (STEM) medium-angle annular dark-field imaging (MAADF) and AFM nanoindentation. We establish a direct correlation by performing the experiments in a vacuum system containing all instruments used [22]. Thus, AFM nanoindentation measurements are performed on atomically clean samples of known

atomic structure. These measurements reveal a significant decrease of E^{2D} with increasing vacancy density. We present a model where the main contribution for the observed softening comes from vacancy-induced corrugation. Molecular dynamics (MD) simulations using machine-learned force fields confirm this corrugation-dominated material softening, and suggest vacancies with two or more missing atoms as the dominant source of the increased corrugation.

The samples were prepared from *Easy Transfer* graphene from Graphenea Inc. and transferred onto custom-designed SiN TEM chips purchased from Silson Ltd. These chips consist of a 200 μm thick Si wafer frame and a 1 μm thick SiN support membrane. The necessity of these custom TEM chips and other details on all methods can be found in the End Matter. Areas suitable for this experiment (*i.e.*, defect-free monolayer) were identified via Raman spectroscopy.

The samples were then inserted into an interconnected vacuum system [22] (through an overnight bake at 160°C), that contains all experimental instruments used here. Surface contamination was removed by illuminating graphene with laser light in ultra-high vacuum (UHV) for several minutes. Next, vacancies were created by Ar^+ ion irradiation at an estimated kinetic energy of < 200 eV. The atomic structure of the defect-engineered graphene was determined by STEM-MAADF imaging at atomic resolution over mesoscopic areas using semi-autonomous imaging at atomic resolution. The microscope was operated at 60 kV. The resulting data was analyzed using a high-throughput technique based on a convolutional neural network (CNN) [23]. AFM nanoindentation was performed to measure the stiffness of defect-engineered graphene using piezo-resistive cantilevers in UHV.

MD simulations were performed using VASP [24] with monoclinic simulation cells with three different lattice vector lengths with periodic boundary conditions on systems that contained different numbers of single or double vacancies. A flat graphene sheet

was initially thermalized, and subsequently pulled step-by-step at room temperature. The two-dimensional elastic modulus was then obtained by fitting the energy-strain curve, as explained in the End Matter.

Samples produced by the liquid transfer method have a high coverage of graphene, as shown in Fig. 1(a). The AFM topography image reveals that all circular perforations are covered by graphene, visible from the height oscillations within the holes. AFM nanoindentation was performed on these graphene-covered holes (graphene drumheads), as shown schematically in Fig. 1(b). The results for E^{2D} of pristine graphene are summarized in Fig. 1(c). The Gaussian distribution has a mean value of 290 ± 27 N/m, which corresponds to a Young's modulus of 868 ± 81 GPa using the interlayer distance of graphite (3.34 Å [25]) as the thickness of graphene. The E^{2D} values are in line with literature [1], although the maximum of our statistical distribution is shifted toward lower values.

The laser light illumination results in most of the graphene lattice being fully exposed, as shown in Fig. 2(a). However, some contamination lines made up of spherical metallic nanoparticles remain visible as bright features in Fig. 2(a). The Ar irradiation of the cleaned graphene [23] introduces vacancies of different types, as shown in Fig. 2(b). Here, graphene takes up the majority of the image, visible as

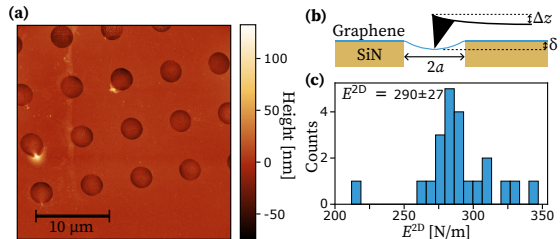


FIG. 1. **AFM nanoindentation of pristine graphene.** (a) AFM topography image of graphene supported by a perforated SiN membrane, (b) schematic illustration of the AFM nanoindentation measurement and (c) distribution of E^{2D} measured on pristine graphene.

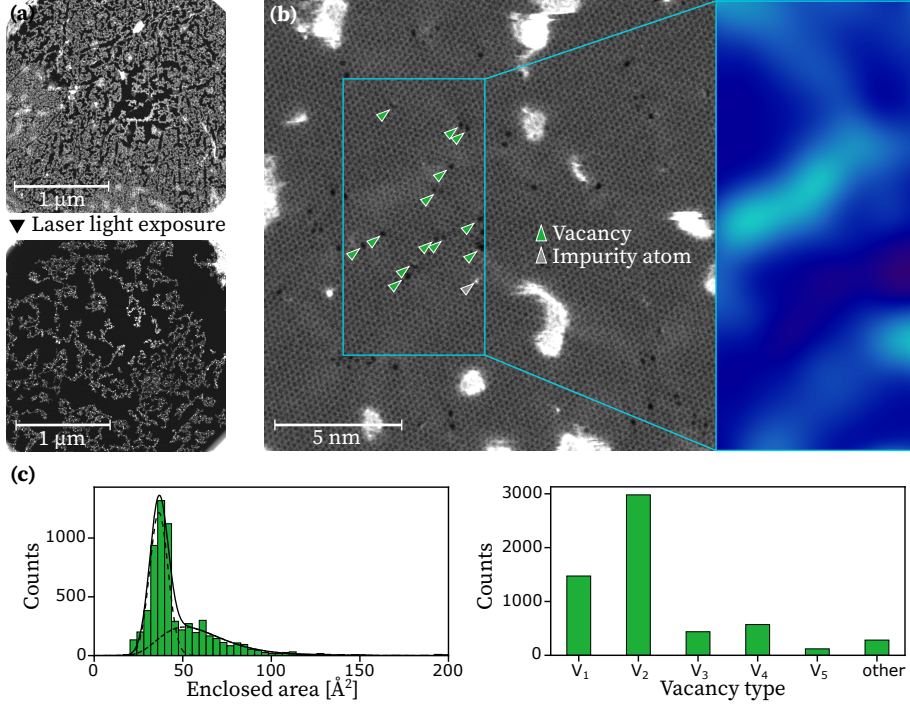


FIG. 2. **Defect-engineered graphene.** (a) STEM-MAADF images of freestanding graphene before and after laser light exposure, (b) near-atomic-resolution STEM-MAADF image of an area with vacancies of different types at an areal density of $4.0 \times 10^{12} \text{ cm}^{-2}$ as well as some impurity atoms. The magnification shown on the right hand side (with a Gaussian blur of 17 px, the original image has 4096×4096 px of which a crop of ca. 1/4 is shown) highlights the morphological roughness. (c) Distributions of the areal sizes of the vacancies and their types across all samples. In the vacancy type distribution the number in the subscript represents the number of missing atoms.

the gray honeycomb lattice. However, the structure is disrupted by missing carbon atoms, *i.e.*, vacancies, that are visible due to the enlarged carbon rings that appear as black spots in the lattice. Occasionally, also some impurity atoms appear embedded in the graphene lattice, visible as bright dots (in Z -contrast images, the brightness scales with the atomic number of the respective element [26]). However, the density of these impurity atoms is negligible compared to the density of introduced vacancies. Some remaining carbon-based contamination is also visible as the bright features of different asymmetric shapes, whose brightness arises from a thickness effect. Finally, it can also be seen that the brightness within the atomically clean

graphene shows subtle spatial variations. This is due to alterations in the projected interatomic distance as seen from the direction of the electron beam, arising from local sample corrugation. This is exemplified by the magnification of the area marked by the turquoise box with applied gaussian blur and false color shown on the right-hand-side of Fig. 2(b).

The images of defect-engineered graphene acquired by semi-automatic image acquisition of mesoscopic areas [23, 27] were quantified in terms of their atomic structure by the CNN-based analyzer with regard to their areal size and the vacancy-type and summarized in Fig. 2(c). Throughout all samples, a total of 5865 vacancies were recognized. For vacancy

densities up to $3.4 \times 10^{13} \text{ cm}^{-2}$, the areal size distributions consist of a Gaussian part and a log-normal part, which is consistent with our previous report [23]. With our irradiation parameters, the most abundant vacancy structures are single and double vacancies. At higher vacancy densities, the data reveals a higher abundance of double vacancies (by a factor of up to 4.4). Toward lower vacancy densities, the number of single vacancies slightly exceeds the number of double vacancies with the largest difference being a factor of 1.6. The individual statistical distributions of each sample can be found in the Supplemental Material [28]. Defects that were only partially visible in the recorded images were neglected in this analysis.

These changes in atomic structure cause a measurable decrease in the mechanical stiffness of graphene [29], which is the opposite of what has previously been reported for low-energy Ar irradiation [13]. Fig. 3(a) shows a force-indentation curve of the same graphene drumhead before and after irradiation (vacancy density of $1.0 \times 10^{13} \text{ cm}^{-2}$). In this case, we find a decrease in E^{2D} from 286 N/m to 158 N/m. Crucially, we consistently find that those graphene drumheads that have been cleaned prior to irradiation have a decreasing E^{2D} with increasing vacancy density, while those that have not, or for which removing the contamination was not entirely successful, have the opposite effect, as shown in Fig. 3(b). Note that for those samples where the atomic structure could not be imaged due to obstruction by contamination, the E^{2D} values are reported as a function of the irradiation time rather than the measured areal density of vacancies. Based on our results, it seems likely that the reported increase in E^{2D} after low-energy ion irradiation [13] is due to contamination build-up [30–38]. However, the decrease in E^{2D} seen in Fig. 3(b) is similar to what has been reported for oxygen plasma irradiation [12], where oxygen plasma is known to etch carbon-based surface contamination [39–44]. Therefore, the latter experiment should indeed correspond to our experiments with atomically clean graphene.

While also most theoretical studies report a

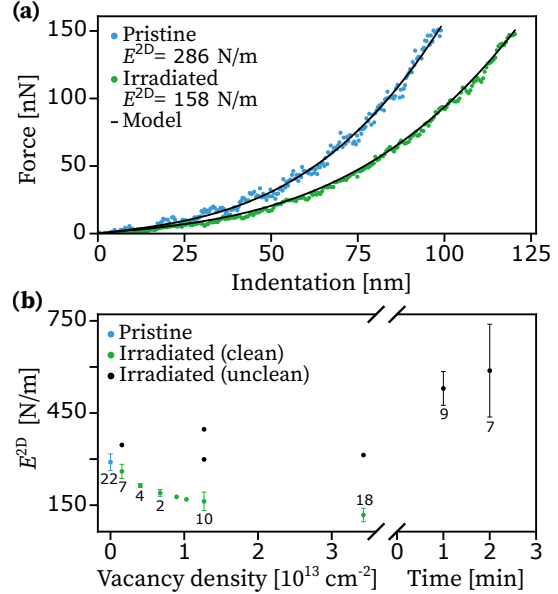


FIG. 3. E^{2D} of defect-engineered graphene. (a) AFM nanoindentation results for the same graphene drumhead before and after the Ar ion irradiation with a fitted model and (b) E^{2D} as a function of vacancy density or irradiation time. The numbers below or above the error bars represent the number of graphene drumheads that have been measured for the corresponding data point. The error bars show the standard deviation.

decrease in E^{2D} with increasing vacancy density [2–11], an increase in E^{2D} similar to the experimental findings of Ref. [13] has also been reported, where the nanoindentation process was simulated on a graphene membrane with a diameter of 13.3 nm [15]. There, the stiffness increase was attributed to enhanced storage of elastic energy in two-coordinated bonds at single- and double-vacancy sites, where the single-vacancies were the main contributor. However, according to the report, when stiffness was estimated using in-plane pulling instead of nanoindentation, this increase was no longer observed. Instead, a linear decrease similar to literature [2–11] was obtained for both vacancy types. As a result, the authors concluded that the stiffness increase observed in the nanoindentation simulation is related to

the local curvature of the graphene membrane induced by the AFM probe. This suggests that the stiffness-increase is a result of the finite size of the simulated graphene membrane, where the area deformed by the tip providing the stiffer two-coordinated bonds dominates the surrounding flat area. In an experiment, however, the graphene membrane is orders of magnitude larger (typically μm), and thus the local area deformed by the tip during loading is negligible compared to the surrounding material. In other words, the experiment has more similarities to the in-plane deformation case and thus one would expect a monotonous decrease in stiffness with increasing vacancy concentration also based on this study.

However, the decrease in E^{2D} observed here is unexpectedly steep and non-linear. Interestingly, a similar steep decrease has been reported to be caused by corrugation of graphene due to small grain sizes or topological defects [16, 17, 20, 21]. Vacancies have been similarly shown to corrugate graphene as a relaxation response to local strain introduced by bond rearrangement [45, 46]. Since STEM-MAADF images (see Fig. 2(b)) suggest the presence of corrugation, we turn to this effect. A more quantitative analysis is presented in Fig. 4(a), where we calculate the image size based on the fast Fourier transform (FFT) of each image and the known lattice constant of graphene, for samples with three different defect densities. All images were recorded with a nominal size of 32 nm. The FFTs are shown in the inset, where each sector corresponds to one of the three STEM-MAADF images. Already the qualitative comparison reveals variations in the distance to the center, visualized by the white dashed lines not perfectly merging at the boundaries of the sectors. As shown in the plot, the quantitative analysis reveals an increase in the apparent image size (or field of view, FOV) with increasing vacancy density. This indicates that more of the lattice appears in images recorded on samples with more vacancies, which can be explained by sample corrugation that results in shorter projected distances between the atoms.

For further insight, we turn to simulations of

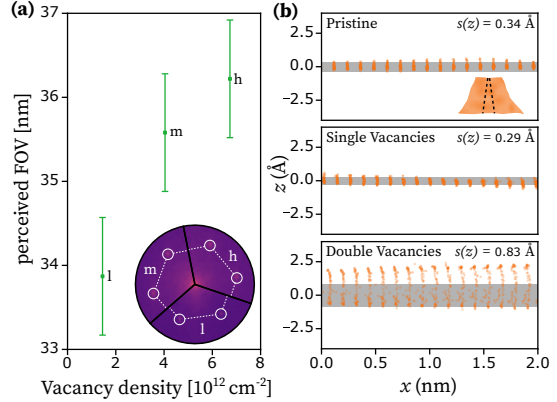


FIG. 4. **Vacancy-induced corrugation.** (a) Rise in the perceived image size (field of view, FOV) with increasing vacancy density. The inset shows the FFTs that were used for calculating the values of FOV at low (l), medium (m) and high (h) vacancy density, each represented by the corresponding sector of the circle. The errorbars correspond to the estimated uncertainty in determining the FOV with this method. (b) Cross-sectional views of exemplary simulated graphene membranes at a vacancy concentration of 0.83%, corresponding to an areal density of $3.2 \times 10^{13} \text{ cm}^{-2}$. The orange dots correspond to carbon atoms while the grey overlay represents their standard deviation in terms of vertical position $s(z)$. The standard deviation has been determined from the entire $12 \times 12 \text{ nm}^2$ membrane while the cross-sectional views are represented by atoms within a 2 nm wide cutout (see inset).

membranes of pristine graphene, graphene with single vacancies and graphene with double vacancies. We consider membranes with periodic boundary conditions in the plane, with an active size of approximately $12 \times 12 \text{ nm}^2$, corresponding to 6,000 atoms for a pristine graphene monolayer equilibrated at 400 K (to accelerate structural relaxation), with the cell being relaxed in the in-plane directions. Fig. 4(b) shows example structures for each case from a cross-sectional view through a 2 nm wide cutout, as illustrated in the inset. Comparing the structures, it is clear that while single vacancies do not introduce any significant corrugation compared to pristine graphene, double vacancies substantially enhance corrugation. Repeating

the simulation for 60 different structures confirms this result. We obtain standard deviations of the out-of-plane coordinate of the atoms ($s(z)$) of 0.36 ± 0.08 Å, 0.35 ± 0.08 Å and 0.64 ± 0.17 Å for pristine graphene, graphene with single vacancies and graphene with double vacancies, respectively.

This observation can be understood based on the Jahn-Teller distortion [47]. In single vacancies, the distortion leads to the formation of one pentagon by bridging together two of the three carbon atoms with a dangling bond. However, at a finite temperature, thermal activation allows this bond to switch between all three possible carbon-carbon pairs so that no direction is preferred. In contrast, the most often found $V_2(585)$ double vacancy [48] is associated with the formation of two such bonds that can only appear in one configuration. This creates a permanent strain in the direction perpendicular to the vacancy axis, which further leads to local corrugation of the lattice. For similar reasons we expect the same behavior for vacancies larger than double vacancies in terms of enhanced corrugation.

Based on this knowledge, we propose a model that incorporates both corrugation effects as well as changes due to the missing atoms into the estimation of E^{2D} with increasing vacancy density

$$E^{2D}(n_{2+}) = E_p^{2D} \times \left(1 - \frac{\overline{N}_m}{C} \frac{n_{2+}}{1.5\rho_A}\right) (R_\varepsilon \alpha \sqrt{n_{2+}} + 1)^{-1}, \quad (1)$$

where E_p^{2D} is the 2D elastic modulus of pristine graphene of 290 ± 27 N/m, n_{2+} is the density of vacancies with at least two missing atoms, $\rho_A = 38.2$ nm⁻² is the atomic areal density of graphene, the factor of 1.5 comes from the fact that every carbon atom contributes 1.5 σ -bonds, $\overline{N}_m = 4.405$ is the average number of missing σ -bonds per vacancy, $C = 0.804$ accounts for the contribution of single vacancies to the missing bonds, $\alpha = 1$ Å is the corrugation amplitude [45], and R_ε is the elastic energy ratio, which is a fitting parameter. Here, \overline{N}_m and C are empirically determined constants

based on the CNN analysis.

While flattening the intrinsic corrugations of free-standing graphene [49–51] doesn't require straining bonds, flattening vacancy-induced corrugation entails straining the bonds within the area of structural disorder. In other words, the corrugated graphene areas around vacancies are in their ground state and thus, in order to flatten it, additional elastic energy has to be applied, which is deposited in said bonds. Therefore, contrary to intrinsic corrugation, vacancy-induced corrugation can be seen as static.

The lower bond density as well as strength of σ -bonds associated with structurally disordered areas compared to pristine graphene results in an effective softening of the material, which is accounted for by R_ε . Fig. 5 shows the model displayed in Eq. (1) applied to the data of clean irradiated graphene, where an $R_\varepsilon = 23.78$ provides a satisfactory fit. The model supports our hypothesis that corrugation is the dominant factor softening graphene. This becomes clear when considering a flat membrane and attributing the reduction in stiffness solely to the missing σ -bonds, *i.e.*, when neglecting the corrugation factor (replacing the last factor in Eq. (1) by 1). This scenario is represented by the dashed line of Fig. 5, where similar to past theoretical studies [2–11] the decrease is much more moderate than the experimental data. Moreover, our model agrees with the findings obtained from simulations concerning the inconsequential impact of single vacancies on the corrugation, as demonstrated in the Supplemental Material [28]. When applying the model on experimental data where single vacancies are included and excluded from the total vacancy density, the latter case provides a much more satisfactory fit compared to the former.

Lastly, the experimental data are compared with the simulation results. As shown in Fig. 5, the simulations reveal that E^{2D} , similar to the experimental findings, decreases with increasing vacancy density. However, the observed reduction is not as large as in the experimental values. We attribute this to finite-size effects due to the periodic boundary conditions used for our simulated membrane (regular, 158.5 nm²),

which may lead to an underestimation of the long-range membrane corrugation (*i.e.*, corrugations with a wavelength exceeding the simulation cell size cannot occur). To demonstrate this, we perform simulations with both larger and smaller membrane sizes (56.6 nm² and 338.0 nm²). As expected, increasing the number of simulated atoms leads to a further decrease in the E^{2D} values. We note that the absolute values of the simulation results for E^{2D} were significantly higher than the experimental values, and a bit higher than values predicted from DFT, and for this reason relative values are shown for the simulation results. We attribute these differences to (i) the approximations in modeling, in particular assuming a perfect, entirely defect-free membrane as the reference value, and to (ii) the approximations within the machine-learned potential. We do not expect any qualitative changes due to these approximations.

In conclusion, we have investigated the impact of vacancies in graphene on its two-

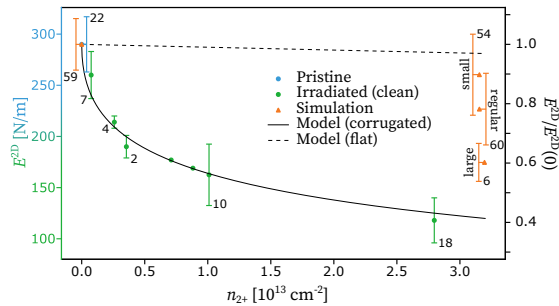


FIG. 5. **Softening due to corrugation.** E^{2D} as a function of the areal density of vacancies with two or more missing atoms (n_{2+}) plotted with two different models for E^{2D} . The number next to each error bar represents the number of measurements acquired for the corresponding data point. The left y -axis represents the experimental values while the right y -axis represents the normalized values with respect to the pristine E^{2D} . At the highest vacancy density simulations were performed for three different membrane sizes. The data points are shown at the correct x -axis position, but in some cases the standard deviations are shifted to make them visible.

dimensional elastic modulus. The atomic structure was analyzed based on atomically resolved STEM images acquired over mesoscopic areas combined with machine-learning-based structure recognition. The introduced defects, predominantly single and double vacancies, result in a decrease of E^{2D} . This reduction in E^{2D} is mainly due to corrugations associated with defects. Atomistic simulations reveal that while single vacancies do not lead to enhanced corrugation, larger vacancy structures significantly corrugate graphene and are therefore the main cause for the softening of defect-engineered graphene. The results also reveal the importance of the removal of surface contamination in preparation for defect engineering, since the opposite effect on E^{2D} is found when the contamination is not removed before irradiating the graphene.

ACKNOWLEDGMENTS

This research was funded in whole or in part by the Austrian Science Fund (FWF) projects [10.55776/P34797, 10.55776/COE5].

END MATTER

Sample preparation The graphene with its Poly(methyl methacrylate) (PMMA) sacrificial layer was put into de-ionized water floating on the water surface. Next, the material was scooped out by the TEM chip followed by subsequent annealing in air at 150°C. Then, the PMMA sacrificial layer was dissolved in an acetone bath at 50°C. The necessity for a custom design stems from the need of a perforated support required for STEM that is also mechanically sufficiently rigid for the normal forces applied during AFM nanoindentation. To the best of our knowledge, the latter is not fulfilled by most commercially available support chips due to lack of thickness of the SiN support membrane, as demonstrated in the Supplemental Material [28], where the divergence between the curves acquired on the rigid Si

wafer frame and the SiN membrane is a result of membrane bending. Comparing the two shows drastically reduced membrane bending on the custom support with 1000 nm thickness and $90 \times 90 \mu\text{m}^2$ wide windows, which is sufficiently low for the forces applied during AFM nanoindentation. Another advantage of the custom design is that the same sample location can be found in each instrument, which is enabled by a binary marker system of the SiN support windows arranged in a 3×3 array, where a missing hole represents a one and an existing hole represents a zero, as shown in the Supplemental Material [28].

Raman spectroscopy The Raman spectroscopy was performed on an alpha300 A developed by WITec GmbH using a 532 nm laser light source at 5 mW of power focused to a probe size of roughly $1 \mu\text{m}$ in diameter, integrated over 0.5 s and accumulated 30 times. The Supplemental Material [28] shows a light microscopy overview image of the sample, where each hole covered by free-standing graphene is classified based on its Raman spectrum, as highlighted in the magnification of the image. Only pristine monolayers are used for this study, which are identified based on evaluation of the G peak (1580 cm^{-1}), the 2D peak ($\approx 2700 \text{ cm}^{-1}$, dispersive) and the D peak ($\approx 1350 \text{ cm}^{-1}$, dispersive) [52]. An example of a graphene drumhead that fulfills these criteria is shown for hole 42 in the Supplemental Material [28].

Interconnected vacuum system The interconnected vacuum system contains a Nion UltraSTEM 100 with a base pressure of 10^{-10} mbar, an AFM device (AFSEM) by Quantum Design GmbH (low 10^{-9} mbar) and a target chamber (low 10^{-10} mbar) with a plasma source used for ion irradiation and a 6 W continuous wave diode laser by Lasertack GmbH with 445 nm wavelength used for contamination removal within UHV [53]. Swift contamination deposition that would occur in ambient conditions [30–32] is prevented by the uninterrupted UHV environment.

Sample cleaning The graphene surface was illuminated with laser light using powers at

17%, 27% or 42% of the maximum device power (depending on the sample). Power adjustments were made in order to minimize the amount of mobile contamination and its electron beam-induced deposition [54–57] by overly excessive heating, that would prevent atomic resolution imaging.

Ar ion irradiation Ion irradiation was performed with a PCS-ECR-HO plasma source developed by SPECS Surface Nano Analysis GmbH. Ar gas was leaked into the target chamber increasing the pressure to 10^{-6} mbar, followed by ionization and acceleration using a magnetron current of 16 mA. The acceleration is purely caused by the sheath potential, resulting in kinetic energies of < 200 eV. The diameter of the divergent beam was estimated to be 9 cm at sample distance, thus a constant flux density was assumed throughout the 3 mm wide sample.

Semi-autonomous STEM acquisition The MAADF detector covered a semi-angular range of 60–200 mrad and the convergence angle of the electron beam was ca. 35 mrad. For each sample, the selected areas in the order of 10^4 nm^2 were defined by four corner points to establish the sample height at all positions through a bilinear interpolation. The selected area was dissected into increments with a nominal size of $5 \times 5 \text{ nm}^2$, which were semi-automatically imaged at atomic resolution. In order to prevent overlap of the imaged areas, an offset of one or two images was used. To minimize residual stage movement during image acquisition, a sleep time of two or three seconds between stage translation and start of the acquisition was implemented.

Mechanical testing The E^{2D} values were determined via AFM nanoindentation using an atomic force microscope. The AFM device uses piezo-resistive cantilevers with Si or single crystal diamond tips. The spring constants were determined by the cantilever geometry, frequency and Q -factor according to the method proposed by Sader *et al.* [58], and ranged from 50 N/m up to 150 N/m. The maximum scan range of $30 \mu\text{m}$ allows locating the individual graphene drumheads through dynamic mode imaging and the

help of the sample map displayed in the Supplemental Material [28]. The E^{2D} was determined through a fit using

$$F(\delta) = (\sigma_0^{2D} \pi) \delta + \left(\frac{E^{2D}}{a^2} \right) \delta^3, \quad (2)$$

where F is the applied force σ_0^{2D} is the pre-tension, a is the radius of the drumhead and δ is the indentation depth of the graphene [1, 13]. Here, E^{2D} and σ_0^{2D} are fit parameters. The indentation depth is calculated as

$$\delta = |z| - \Delta z, \quad (3)$$

with z being the height of the z -piezo position relative to its contact point position and Δz being the vertical deflection of the cantilever.

Molecular dynamics simulation A machine learning force field, trained via active learning for distorted and ruptured membranes, was developed for a total of 12,000 MD steps over 12 different membrane systems and a total of 585 configurations evaluated by density functional theory (DFT) using the Perdew–Burke–Ernzerhof functional [59]. Periodic boundary conditions in all directions were applied. To prevent interactions along the surface normal of the graphene sheet a vacuum of approximately 6 nm was introduced. A total of 60 simulations per vacancy density were per-

formed. Each simulation started with a perfectly flat graphene sheet and a temperature of $T = 400$ K (to accelerate the built-up of corrugation) in an isobaric-isothermal ensemble (NPT) using a Langevin thermostat. The system was then equilibrated until the average corrugation no longer increased, which required 20 ps in the case of pristine graphene and 40 – 60 ps for defective graphene. This was followed by 0.3 ps of damped MD to relax the system, in order to obtain a good starting point for the subsequent procedure. Subsequently, the membrane was pulled at $T = 300$ K by incrementally enlarging the in-plane cell size. This included a total of 20 strain steps, where in each step the in-plane cell size was increased by 0.05%. Each step was simulated for 10 ps, in order to ensure that the system has sufficient time to adapt to the increased volume. The standard deviation of the atomic heights distribution was determined at each time step. This distribution was sampled over all atoms and simulated systems. The two-dimensional elastic modulus was then obtained by fitting the energy-strain curve with

$$\frac{E(\epsilon_A) - E_0}{A_0} = \frac{E^{2D}}{4} \epsilon_A^2, \quad (4)$$

where ϵ_A denotes the strain related to the area of the membrane, A_0 is the area of the membrane and E_0 corresponds to the energy of the relaxed membrane.

-
- [1] C. Lee, X. Wei, J. W. Kysar, and J. Hone, *Science* **321**, 385 (2008).
- [2] F. Hao, D. Fang, and Z. Xu, *Applied Physics Letters* **99**, 041901 (2011).
- [3] A. Ito and S. Okamoto, *Engineering Letters* **20** (2012).
- [4] B. Mortazavi, S. Ahzi, V. Toniazzo, and Y. Rémond, *Physics Letters A* **376**, 1146 (2012).
- [5] A. Tapia, R. Peón-Escalante, C. Villanueva, and F. Avilés, *Computational Materials Science* **55**, 255 (2012).
- [6] N. Jing, Q. Xue, C. Ling, M. Shan, T. Zhang, X. Zhou, and Z. Jiao, *RSC Adv.* **2**, 9124 (2012).
- [7] K. Tserpes, *Acta Mechanica* **223**, 669–678 (2012).
- [8] R. Dettori, E. Cadelano, and L. Colombo, *Journal of Physics: Condensed Matter* **24**, 104020 (2012).
- [9] B. Mortazavi and S. Ahzi, *Carbon* **63**, 460 (2013).
- [10] Q. H. Yingjing Liang and S. Huan, *Journal of Thermal Stresses* **38**, 926 (2015).

- [11] M. Li, T. Deng, B. Zheng, Y. Zhang, Y. Liao, and H. Zhou, *Nanomaterials* **9**, 347 (2019).
- [12] A. Zandiatashbar, G. H. Lee, S. J. An, S. Lee, N. Mathew, M. Terrones, T. Hayashi, C. R. Picu, J. Hone, and N. Koratkar, *Nature Communications* **5**, 3186 (2014).
- [13] G. López-Polín, C. Gómez-Navarro, V. Parente, F. Guinea, M. I. Katsnelson, F. Pérez-Murano, and J. Gómez-Herrero, *Nature Physics* **11**, 26 (2015).
- [14] L. Chu, J. Shi, and R. Braun, *Physica E: Low-dimensional Systems and Nanostructures* **110**, 115 (2019).
- [15] D. Kvashnin and P. Sorokin, *The Journal of Physical Chemistry Letters* **6**, 2384 (2015).
- [16] H. Qin, Y. Sun, J. Z. Liu, and Y. Liu, *Carbon* **108**, 204 (2016).
- [17] J. W. Suk, Y. Hao, K. M. Liechti, and R. S. Ruoff, *Chemistry of Materials* **32**, 6078 (2020).
- [18] Z. Dai, G. Wang, Z. Zheng, Y. Wang, S. Zhang, X. Qi, P. Tan, L. Liu, Z. Xu, Q. Li, Z. Cheng, and Z. Zhang, *Carbon* **147**, 594 (2019).
- [19] A. G. Kvashnin, P. B. Sorokin, and D. G. Kvashnin, *Fullerenes Nanotubes and Carbon Nanostructures* **18**, 497 (2010).
- [20] C. S. Ruiz-Vargas, H. L. Zhuang, P. Y. Huang, A. M. Van Der Zande, S. Garg, P. L. McEuen, D. A. Muller, R. G. Hennig, and J. Park, *Nano Letters* **11**, 2259 (2011).
- [21] R. Wang, H. Pang, M. Li, and L. Lai, *Materials* **13**, 1127 (2020).
- [22] C. Mangler, J. Meyer, A. Mittelberger, K. Mustonen, T. Susi, and J. Kotakoski, *Microsc. Microanal.* **28**, 2940 (2022).
- [23] A. Trentino, J. Madsen, A. Mittelberger, C. Mangler, T. Susi, K. Mustonen, and J. Kotakoski, *Nano Letters* **21**, 5179 (2021).
- [24] G. Kresse and J. Furthmüller, *Phys. Rev. B* **54**, 11169 (1996).
- [25] Y. Baskin and L. Meyer, *Phys. Rev.* **100**, 544 (1955).
- [26] O. Krivanek, T. Lovejoy, and N. Dellby, *Journal of microscopy* **259**, 165 (2015).
- [27] A. Mittelberger, *Electron microscopy imaging of radiation-sensitive specimens with atomic resolution*, Ph.D. thesis, University of Vienna (2018).
- [28] See Supplemental Material at [HYPERLINK](#) for additional figures regarding custom TEM chips and their rigidity, Raman spectroscopy pre-characterization, statistical distributions of the vacancy sizes and types and a comparison of the proposed model applied to experimental data with and without considering single vacancies.
- [29] W. Joudi, A. Trentino, K. Mustonen, C. Mangler, and J. Kotakoski, *Microscopy and Microanalysis* **28**, 2626 (2022).
- [30] Z. Li, A. Kozbial, N. Nioradze, D. Parobek, G. J. Shenoy, M. Salim, S. Amemiya, L. Li, and H. Liu, *ACS Nano* **10**, 349 (2016).
- [31] Z. Li, Y. Wang, A. Kozbial, G. J. Shenoy, F. Zhou, R. McGinley, P. A. Ireland, B. Morganstein, A. Kunkel, S. P. Surwade, L. Li, and H. Liu, *Nature materials* **10**, 349 (2013).
- [32] C. Amadei, C.-Y. Lai, D. Heskes, and M. Chiesa, *The Journal of chemical physics* **141**, 084709 (2014).
- [33] A. Kozbial, Z. Li, J. Sun, X. Gong, F. Zhou, Y. Wang, H. Xu, H. Liu, and L. Li, *Carbon* **74**, 218 (2014).
- [34] A. Kozbial, Z. Li, C. Conaway, R. McGinley, S. Dhingra, V. Vahdat, F. Zhou, B. Durso, H. Liu, and L. Li, *Langmuir* **30**, 8598 (2014).
- [35] A. Ashraf, Y. Wu, M. C. Wang, N. R. Aluru, S. A. Dastgheib, and S. Nam, *Langmuir* **30**, 12827 (2014).
- [36] Y. Wei and C. Q. Jia, *Carbon* **87**, 10 (2015).
- [37] C. Mücksch, C. Rösch, C. Müller-Renno, C. Ziegler, and H. M. Urbassek, *The Journal of Physical Chemistry C* **119**, 12496 (2015).
- [38] P. J. Smith and P. M. Lindley, *AIP Conference Proceedings* **449**, 133 (1998).
- [39] P. Ponath, A. Posadas, R. Hatch, and A. Demkov, *Journal of Vacuum Science Technology B: Microelectronics and Nanometer Structures* **31**, 031201 (2013).
- [40] M. Baker, *Thin Solid Films* **69**, 359 (1980).
- [41] L. Chan, E. Altman, and Y. Liang, *Journal of Vacuum Science Technology A* **19**, 976 (2001).
- [42] C. Oh, F. Streller, W. R. Ashurst, R. W. Carpick, and M. P. D. Boer, *Journal of Micromechanics and Microengineering* **26**, 115020 (2016).
- [43] T. C. Isabell, P. E. Fischione, C. O’Keefe, M. U. Guruz, and V. P. Dravid, *Microscopy and Microanalysis* **5**, 126 (1999).
- [44] H. Li, A. Belkind, F. Jansen, and Z. Orban, *Surface and Coatings Technology* **92**, 171 (1997).
- [45] J. Kotakoski, F. R. Eder, and J. C. Meyer, *Phys. Rev. B* **89**, 201406 (2014).
- [46] F. L. Thiemann, P. Rowe, A. Zen, E. A. Müller, and A. Michaelides, *Nano Letters* **21**, 8143 (2021).

- [47] R. Babar and M. Kabir, *Phys. Rev. B* **98**, 075439 (2018).
- [48] F. Banhart, J. Kotakoski, and A. V. Krasheninnikov, *ACS Nano* **5**, 26 (2011).
- [49] J. Meyer, A. Geim, M. Katsnelson, K. Novoselov, T. Booth, and S. Roth, *Nature* **446**, 60 (2007).
- [50] A. Fasolino, J. H. Los, and M. I. Katsnelson, *Nature Materials* **6**, 858 (2007).
- [51] R. Singh, D. Scheinecker, U. Ludacka, and J. Kotakoski, *Nanomaterials* **12**, 3562 (2022).
- [52] A. Ferrari, J. Meyer, V. Scardaci, C. Casiraghi, M. Lazzeri, F. Mauri, S. Piscanec, D. Jiang, K. Novoselov, S. Roth, and A. Geim, *Physical review letters* **97**, 187401 (2006).
- [53] M. Tripathi, A. Mittelberger, K. Mustonen, C. Mangler, J. Kotakoski, J. C. Meyer, and T. Susi, *physica status solidi (RRL) - Rapid Research Letters* **11**, 1700124 (2017).
- [54] O. Dyck, S. Kim, S. V. Kalinin, and S. Jesse, *Journal of Vacuum Science Technology B* **36**, 011801 (2017).
- [55] R. Egerton, P. Li, and M. Malac, *Micron* **35**, 399 (2004).
- [56] C. M. McGilvery, A. E. Goode, M. S. Shaffer, and D. W. McComb, *Micron* **43**, 450 (2012).
- [57] O. Dyck, A. Okmi, K. Xiao, S. Lei, A. R. Lupini, and S. Jesse, *Advanced Materials Interfaces* , 2400598 (2024).
- [58] J. Sader, J. Chon, and P. Mulvaney, *Review of Scientific Instruments* **70**, 3967–3969 (1999).
- [59] J. P. Perdew, K. Burke, and M. Ernzerhof, *Phys. Rev. Lett.* **77**, 3865 (1996).

SUPPLEMENTAL MATERIAL

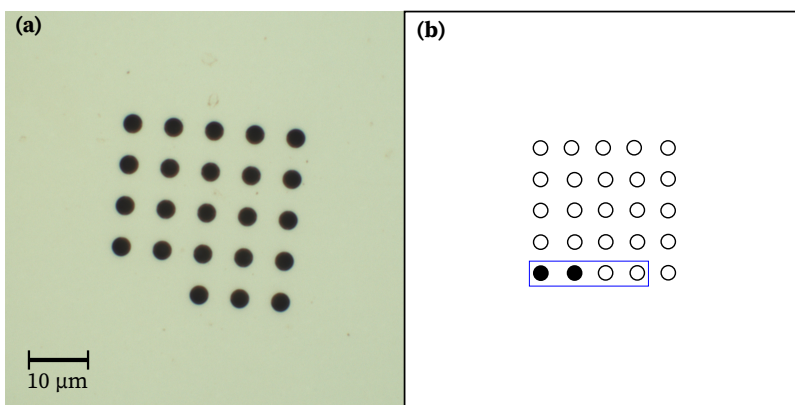


FIG. S 1. **Finder grid.** (a) Visible light microscopy image of perforated SiN support membrane at $100\times$ magnification and (b) sketch explaining the binary marking system (1100 corresponds to 3).

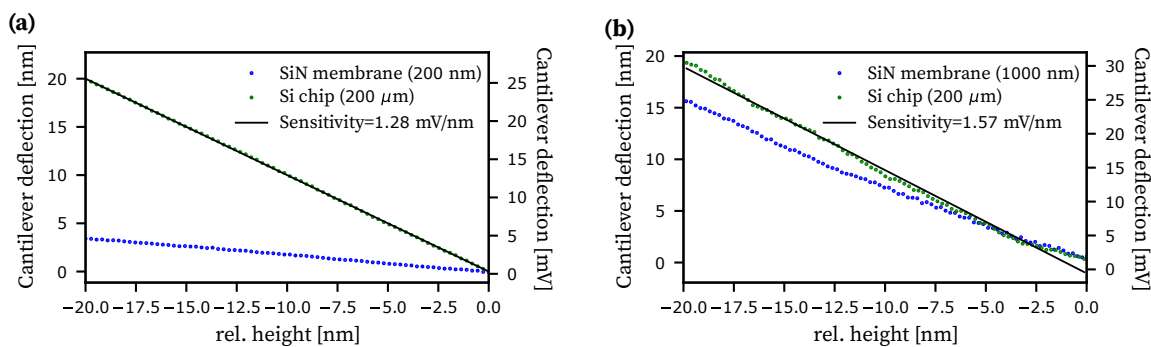


FIG. S 2. **Support membrane rigidity.** (a) Comparison of force-distance curves acquired on Si frame ($200\ \mu\text{m}$) and perforated SiN support membrane ($500 \times 500\ \mu\text{m}^2$, 200 nm thick) performed on commercially available PELCO holey SiN support film for TEM by Ted Pella, Inc. (b) Comparison of force-distance curves acquired on Si frame ($200\ \mu\text{m}$) and perforated SiN support membrane ($90 \times 90\ \mu\text{m}^2$, 1000 nm thick) performed on custom SiN TEM support chip by Silson Ltd.

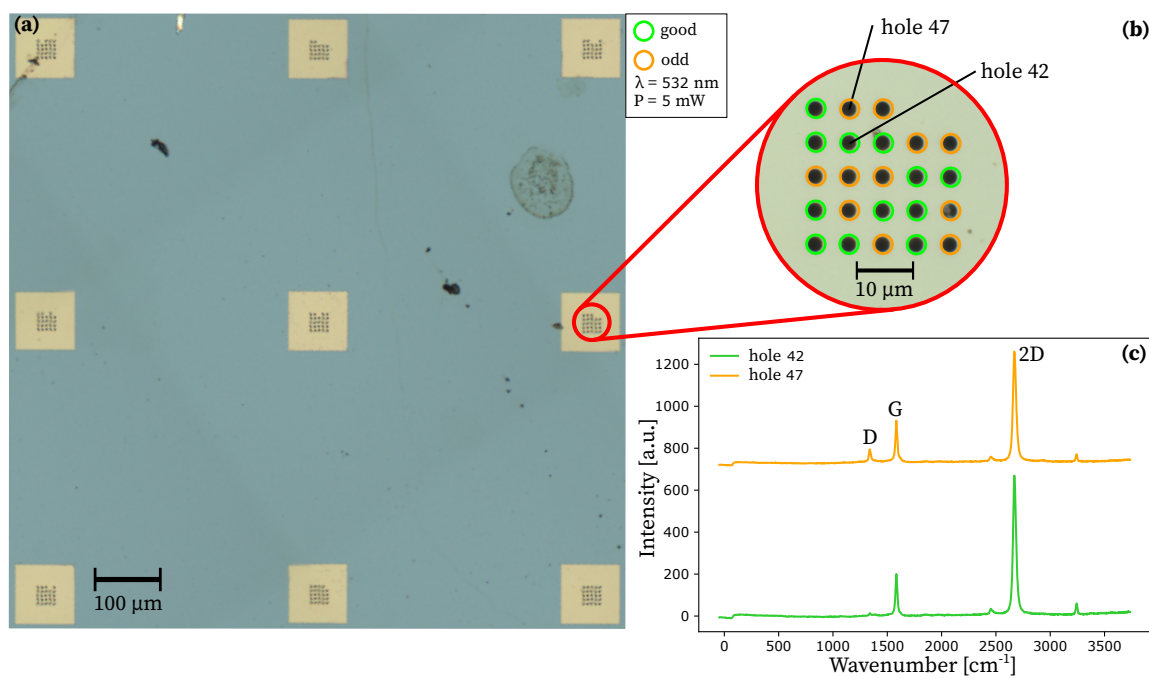
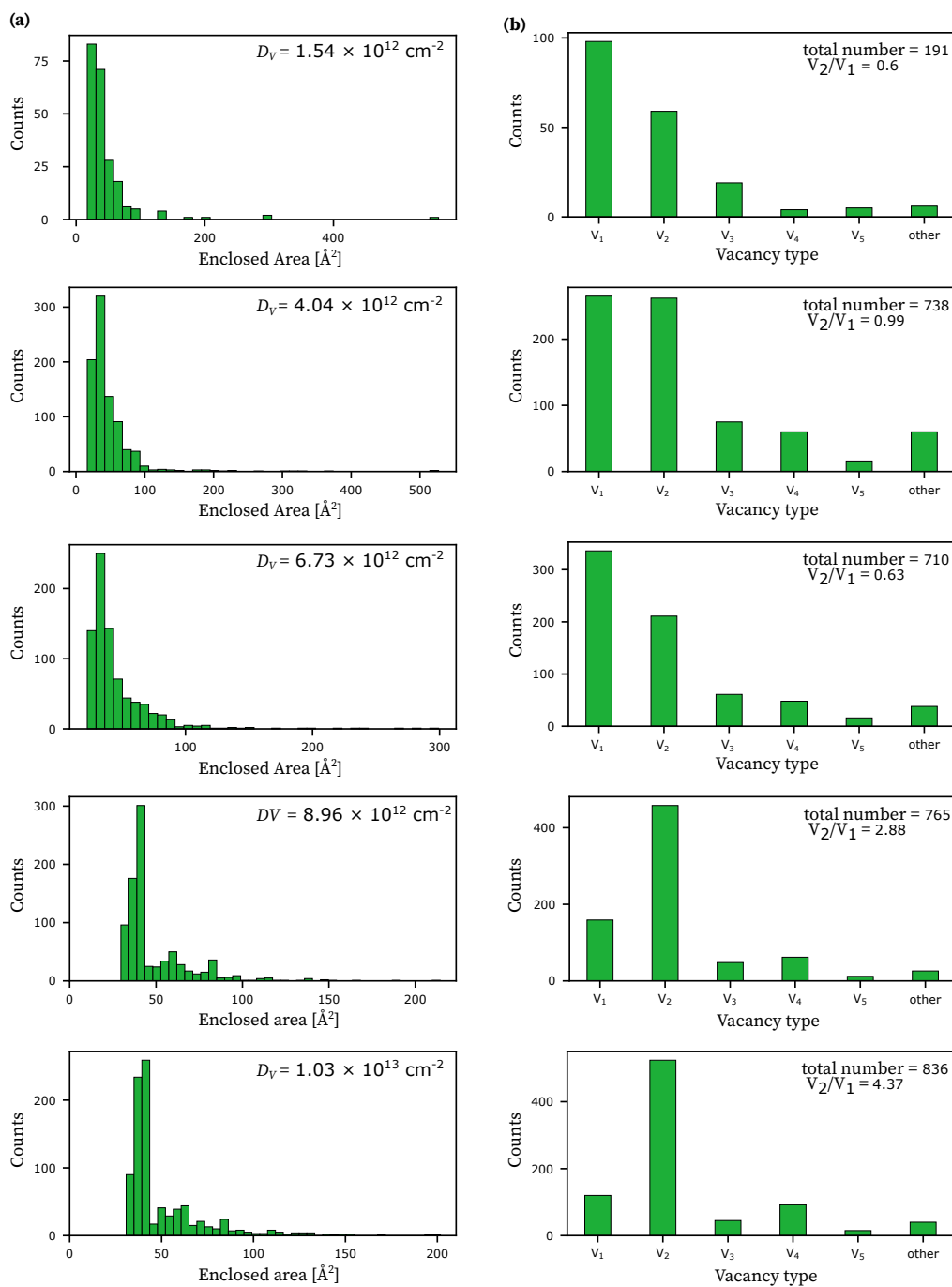


FIG. S 3. **Raman pre-characterization.** (a) Visible light microscopy image of the sample, (b) magnified image of SiN support window with coloured overlay indicating the quality of the free-standing graphene above each hole and (c) corresponding example Raman spectra used for determining the local graphene quality.



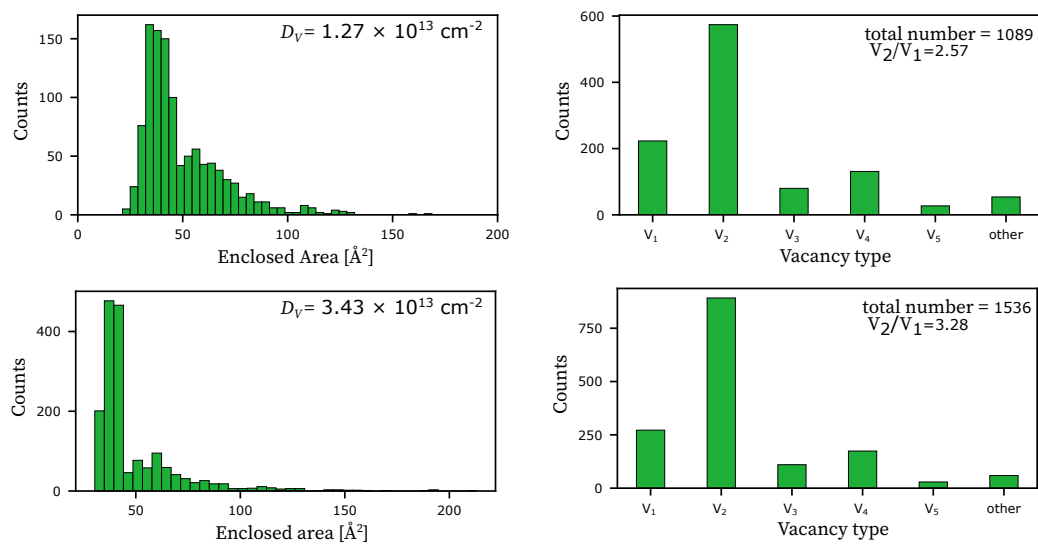


FIG. S 4. **Vacancy distributions.** (a) Areal size distribution of the vacancies that were introduced into the the lattice, where the size is quantified by the area that is enclosed within the vacancy. D_V represents the vacancy density of the corresponding sample. (b) Vacancy-type distribution, where the subscript represents the number of missing carbon atoms in the respective vacancy structure.

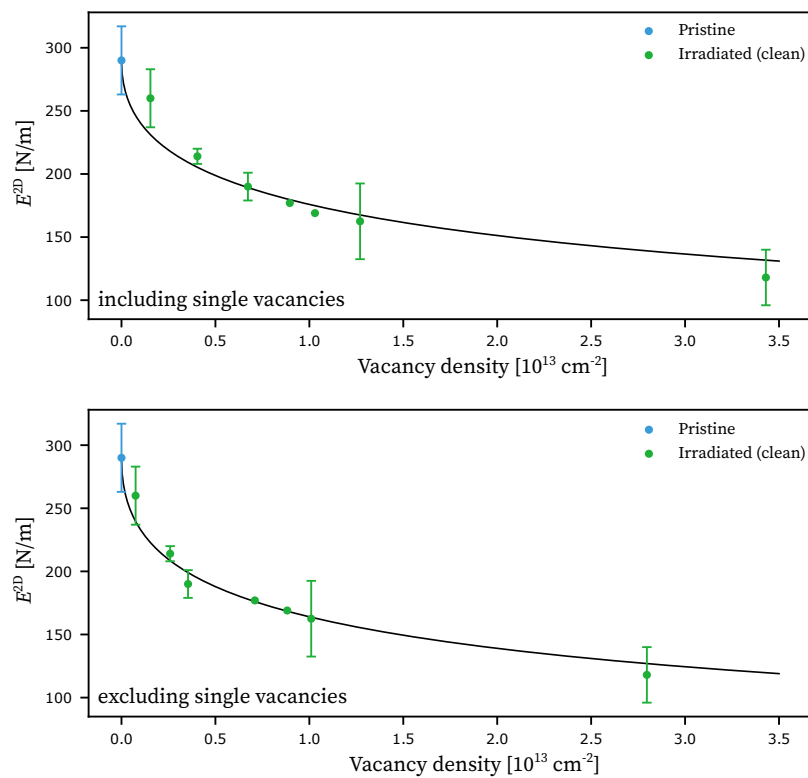


FIG. S 5. **Vacancy type effect.** Model accounting for corrugation compared to data where single vacancies have been included in (top) and excluded from (bottom) the total vacancy density.